scientific reports

Check for updates

OPEN

Core–shell structured silver-ferrite nanoparticles for antibacterial action and magnetic removal of bacteria from aqueous media

Ágnes Mária Ilosvai[1,2], Orsolya Alberti[1,2], Karina Kecskés[1,2], Lajos Daróczi[3], Ferenc Kristály[4], Miklós Nagy[1], Béla Viskolcz[1,2], Emma Szőri-Dorogházi[1,2]✉ & László Vanyorek[1]✉

In this work, we synthesized antibacterial core-shell structured magnetic nanoparticles with silver particles as the core and nickel-ferrite or cobalt-ferrite crystallites as the shell using solvothermal method. The prepared ferromagnetic amine-functionalized Ag/$NiFe_2O_4$ and Ag/$CoFe_2O_4$ particles had a saturation magnetization (Ms) of 40 emu/g and 37 emu/g, respectively, and were therefore easily separated from aqueous media by magnetic field, thus making them excellent magnetic adsorbents. The produced core-shell particles had mean diameters of 276 ± 70 nm (Ag/$CoFe_2O_4$) and 337 ± 109 nm (Ag/$NiFe_2O_4$). Due to their silver content, these particles showed outstanding antibacterial activity against Gram-positive (*Micrococcus luteus*) and Gram-negative (*Escherichia coli*) bacteria, which was confirmed by bacteriological studies. For *E. coli*, a nanoparticle concentration of less than 0.5 mg/mL was sufficient to inhibit growth on solid surfaces, whereas for *M. luteus* a concentration of 3 mg/mL was effective. This difference in antibacterial efficacy can be explained by differences in the cell wall structure of Gram-negative and Gram-positive bacteria. In addition to being effective in killing bacteria, both types of Ag-containing magnetic nanoparticles also exhibited excellent adsorption capacity, removing 100% of microorganisms from the tested solution. In liquid-phase assays, complete antibacterial and adsorptive efficacy was achieved at 1.0 mg/mL for *E. coli* with Ag/$CoFe_2O_4$, while Ag/$NiFe_2O_4$ reached full efficiency at concentrations as low as 0.1 mg/mL; for *M. luteus*, both 1.0 and 3.0 mg/mL proved fully effective. Time-kill kinetic tests further confirmed the rapid action of the nanoparticles, with total bacterial elimination occurring within 10 min. This rapid and high removal efficiency is likely attributed to the silver content and positive surface charge of the magnetic particles, which facilitates electrostatic interactions with the negatively charged bacterial membranes. Given their strong antibacterial and adsorption performance demonstrated in our experiments, these nanoparticles are highly promising candidates for water treatment applications in the future.

Keywords Antibacterial nanoparticles, Core-shell nanostructures, Magnetic separation, Water purification

Magnetic nanoparticles (MNPs) are currently receiving considerable attention due to their superior magnetic characteristics[1]. The field of biomedicine should be highlighted, where magnetic nanoparticles are being investigated in applications such as targeted drug delivery, magnetic resonance imaging (MRI), DNA isolation or magnetic hyperthermia[2–7].

Magnetic nanoparticles can be iron oxide, ferrite or core-shell nanoparticles[8–10]. Ferrite nanoparticles are oxides with a magnetic spinel structure, consisting mainly of a combination of iron and other metals such as cobalt, manganese, nickel or zinc. Their general formula is MFe_2O_4, where M may denote a different metal ion[11,12]. Several synthesis methods are known to produce ferrite nanoparticles, such as co-precipitation, hydrothermal/solvothermal, microwave synthesis, etc[13–15]..

[1]Institute of Chemistry, University of Miskolc, Miskolc-Egyetemváros, Miskolc H- 3515, Hungary. [2]Higher Education and Industrial Cooperation Centre, University of Miskolc, Miskolc H-3515, Hungary. [3]Department of Solid State Physics, University of Debrecen, P.O. Box 2, Debrecen H- 4010, Hungary. [4]Institute of Mineralogy and Geology, University of Miskolc, Miskolc H-3515, Hungary. ✉email: emma.szdoroghazi@uni-miskolc.hu; laszlo.vanyorek@uni-miskolc.hu

The coprecipitation method is the most widely used manufacturing method for producing high-purity and high-volume magnetic nanoparticles. In this process, the appropriate materials are weighed and poured step by step into a flask where they are refluxed at high temperature and with continuous stirring[16,17]. However, the disadvantage of the co-precipitation synthesis method is that the particle size and morphology of the particles cannot necessarily be controlled, the resulting particles are prone to aggregation and the process does not result in a perfect crystal structure[18,19].

Hydrothermal/solvothermal synthesis uses high pressure and temperature and is a time-consuming process. The synthesis method employs a Teflon-lined autoclave in which the material is heated at a defined temperature (typically at 200 °C) for a defined period of time (usually ~ 12–20 h)[20,21]. Compared to co-precipitation synthesis, hydrothermal synthesis produces particles with better controllability and higher crystallinity, which can enhance the magnetic properties of the material. As a result, such materials can be used in catalysis, electronics and biomedical applications[22,23]. Controlling the particle size is important because magnetic nanoparticles change their magnetic properties below a certain particle size, i.e. transition from ferromagnetic to paramagnetic behavior can occur. Moreover, the degree of crystallinity significantly influences magnetic properties by affecting the arrangement of magnetic moments and the formation of magnetic domains. Due to these considerations, we chose the solvothermal synthesis method for preparing our ferrites.

As discussed earlier, core-shell nanoparticles can also be produced in addition to ferrites. Core-shell nanoparticles are nanostructures consisting of a central core surrounded by one or more outer layers. The core and shell can be composed of different materials: for example, the core may be a noble metal (Au, Ag) or magnetite (Fe_3O_4), while the shell can be silica or another polymer[10,24]. It is also possible to design structures where the core is Au and the shell is composed of ferrite nanoparticles. The material difference between the core and the shell enables the combination of the unique properties of each component, thereby broadening the range of potential applications[27].

Just as gold can serve as the core material in such structures, another precious metal, namely silver, can be used with equal effectiveness. Ferrite particles provide magnetic properties, while silver contributes antibacterial activity; thus, combining these two materials yields antibacterial nanoparticles that can be manipulated using an external magnetic field[28,29]. Magnetite can also be employed effectively as a coating material for antibacterial silver nanoparticles. The resulting magnetic core-shell structures have been shown to exhibit superior antimicrobial efficacy against pathogenic microorganisms like *Salmonella typhimurium* and *Escherichia coli*[29]. Building on these properties, silver-containing magnetic nanoparticles (Ag/MNPs) are increasingly explored for practical applications, particularly in water purification[30–32]. Their high surface-to-volume ratio enhances bacterial interaction, enabling effective removal of both Gram-positive and Gram-negative bacteria, including antibiotic-resistant strains[33–35]. In addition to microbial disinfection, their high reactivity and sorption capacity toward organic pollutants and heavy metals (e.g. antimony) also make them suitable for industrial wastewater treatment[36], well water and groundwater purification[37,38]. Unlike conventional disinfectants, silver nanoparticles do not produce harmful by-products and show antimicrobial activity primary under aerobic conditions[39–41]. They show strong potential for use as point-of-use technologies in water treatment systems. Their magnetic properties allow for easy separation and recovery from treated water, making them both cost-effective and reusable[37].

To utilize the antimicrobial properties of nanomaterials different amine-functionalized MNPs ($NiFe_2O_4$, $CoFe_2O_4$, Ag/$NiFe_2O_4$, Ag/$CoFe_2O_4$) were synthesized, characterized and evaluated for their ability to inhibit bacterial growth and remove both Gram-negative *(Escherichia coli)* and Gram-positive (*Micrococcus luteus*) bacterial cells from suspension. Their effectiveness in removing microorganisms from solution was also assessed. The long-term aim of this study is to explore the potential application of these nanomaterials in water treatment systems as a practical, efficient, and economical disinfection approach.

Results and discussion

Characterization of the amine-functionalized $NiFe_2O_4$ and $CoFe_2O_4$ samples

After the solvothermal synthesis and purification of the amine-functionalized magnetic nanoparticles (MNPs), their particle size and morphology were investigated by TEM examinations. The TEM images of the cobalt- and nickel ferrites show spherical particles (Fig. 1A and B). The average particle diameters were 216 ± 34 nm ($CoFe_2O_4$) and 292 ± 40 nm ($NiFe_2O_4$) (Fig. 1C). These spherical polycrystallites are composed of smaller crystallites with sizes between 5 and 25 nm, according to XRD measurements.

Elemental mapping analyses were performed to investigate the elemental composition and distribution in the samples. The elemental maps clearly show the presence of the corresponding transition metals, as well as iron and oxygen, as constituents of the ferrites (Fig. 2). It can be seen that the spatial distributions of the three ferrite constituent elements coincide, indicating that the metals are not present in elemental form or other compounds, only transition metal ferrites are found in both samples.

The formation of the ferrite crystal phase, typical of spinel structures, after synthesis was confirmed by selected area electron diffraction (SAED) measurements. Based on the SAED results, according to the measured d-spacing values, the (111), (220), (311), (400), (422), (511) and (440) reflections correspond to characteristic planes of the ferrite structures of the $CoFe_2O_4$ (PDF 22–1086) and $NiFe_2O_4$ (PDF 10–0325) (Fig. 3A and B). Energy dispersive X-ray (EDX) spectra were recorded to check for the presence of undesired compounds (contaminants) besides ferrites in the samples. The EDX spectra show peaks of iron, oxygen and the transition metals corresponding to each ferrite (Fig. 3C and D). EDX also shows a peak characteristic of carbon, which may be due to organic molecules adsorbed on the ferrite particle surfaces during synthesis or may indicate the carbon coating of the sample support grid (Ted Pella TEM Grids: Lacey Carbon Type A on 300 mesh, Copper). The presence of copper peak is due to the TEM grid material. No impurities (such as inorganic salts or metals) were observed in the spectra, indicating that the samples contain only ferrites.

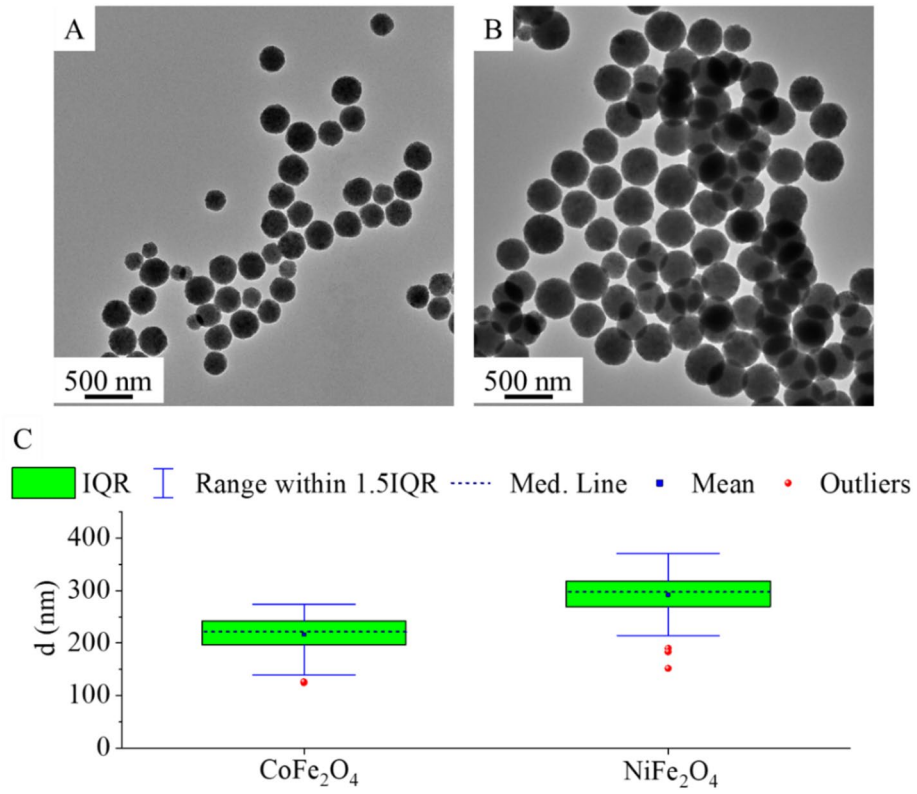

Fig. 1. TEM pictures of the amine-functionalized $CoFe_2O_4$ (**A**), $NiFe_2O_4$ (**B**) MNPs, and box-plot diagrams of the particle size distributions (**C**).

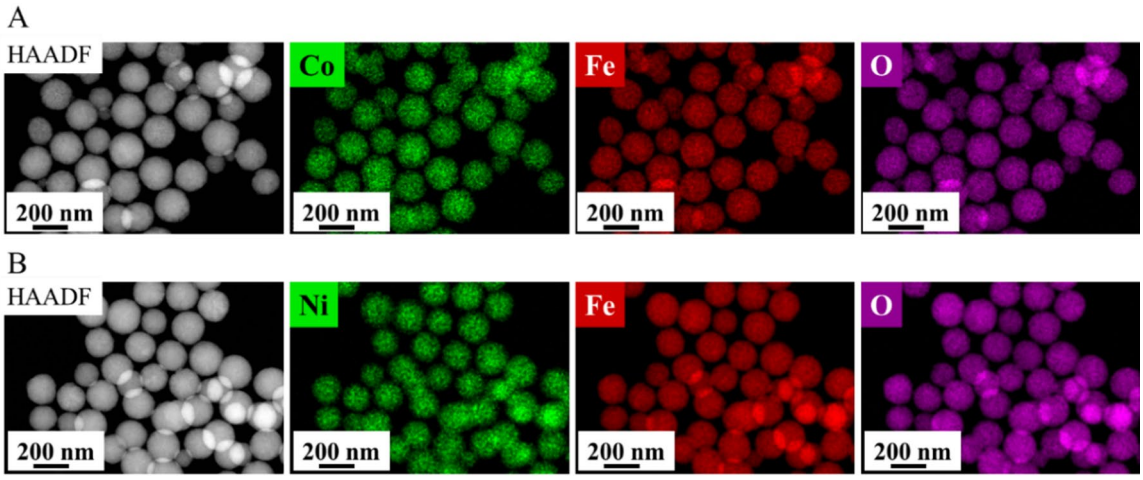

Fig. 2. HAADF picture and element maps of the amine-functionalized $CoFe_2O_4$ (**A**) and $NiFe_2O_4$ (**B**) samples.

In the X-ray diffractogram of the $CoFe_2O_4$ sample, reflection peaks were located at 18.2° (111), 29.9° (220), 35.5° (311), 43.1° (400), 53.6° (422), 57.2° (511) and 62.7° (440) two theta degrees, which corresponds to cobalt ferrite (PDF 22–1086) (Fig. 4A). Another metal oxide phase was found in the sample, namely magnetite. The characteristic reflexions of the magnetite were identified at 18.3° (111), 30.2° (220), 35.6° (311), 43.4° (400), 53.8° (422), 57.4° (511), and 63.0° (440), with two theta degrees (PDF 19–0629). Besides cobalt ferrite, 7.2 wt% magnetite was detected as a magnetic by-product. Based on the XRD results, the crystallite sizes were calculated using the full width at half maximum (FWHM) method. The average crystallite sizes were 13 ± 2 nm ($CoFe_2O_4$) and 25 ± 5 nm (Fe_3O_4).

In case of the nickel ferrite sample, (111), (220), (311), (400), (422), (511) and (440) reflexions were identified at 18.1°, 30.1°, 35.5°, 43.2°, 53.8°, 57.2° and 62.8° two theta degrees, which belong to the spinel structure of the

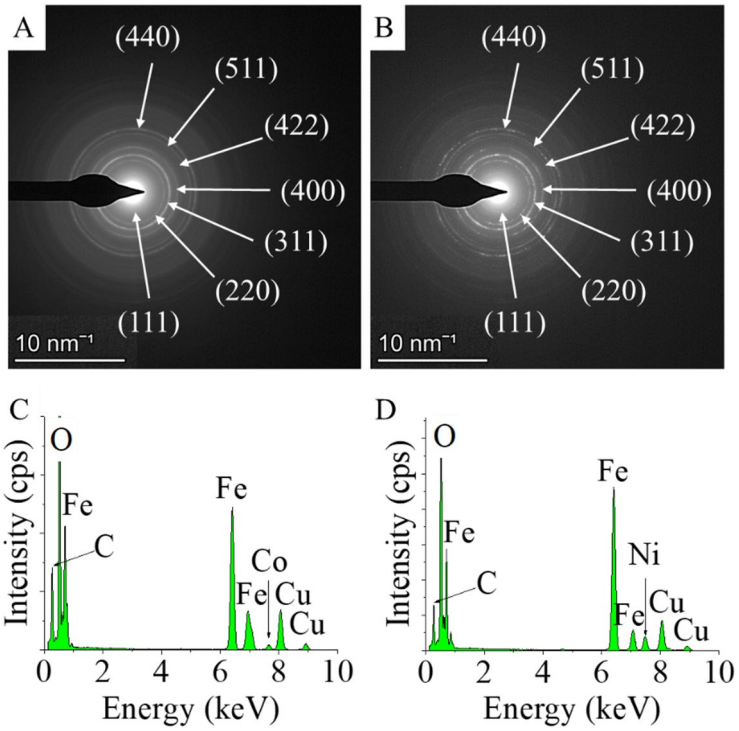

Fig. 3. SAED picture and EDX spectrum of the amine-functionalized $CoFe_2O_4$ (**A**, **C**) and $NiFe_2O_4$ (**B**, **D**) samples.

non-stoichiometric ($Ni_{1.43}O_{1.7}O_4$) nickel ferrite (PDF 10–0325) (Fig. 4B). In addition to nickel ferrite, magnetite is also found, similarly to the cobalt ferrite sample. In this case the amount of magnetite was 2.1 wt%. Based on the XRD results, the average crystallite sizes were 8 ± 2 nm ($Ni_{1.43}Fe_{1.7}O_4$) and 28 ± 6 nm (Fe_3O_4).

Vibrating-sample magnetometer (VSM) measurements were performed on the amine-functionalized ferrite MNPs, at 303 K. The maximum magnetic saturation (Ms) value (73 emu/g) was reached in case of $CoFe_2O_4$ sample, which is close to the reported value for the bulk samples (80 emu/g) and the $NiFe_2O_4$ showed 57 emu/g Ms value, which is close to the theoretical value of (bulk material) 50 emu/g (Fig. 5A and B)[42,43]. As mentioned above, the average size of the $NiFe_2O_4$ and $CoFe_2O_4$ were 292 ± 40 nm and 216 ± 34 nm, respectively. These spherical particles are composed of crystallites of a few nanometres (5–10 nm) in size. Due to the smaller size, the finite-size effect becomes more pronounced, resulting in a lower saturation magnetization for the nanoparticles compared to the bulk phase[44]. The magnetization curves of the ferrite samples show a narrow hysteresis loop with coercivity (Hc) 197 Oe ($CoFe_2O_4$) and 67 Oe ($NiFe_2O_4$) with 11.3 emu/g and 5.7 emu/g remanent magnetization (Mr) as can be seen in the inlets of VSM curves on Fig. 5. The measured values of Hc and Mr of the two samples indicates the ferromagnetic nature of the synthesized particles at room temperature. Narrow hysteresis loops indicate that the prepared sample can be easily demagnetized.

The residual magnetization (Ms: 73 emu/g) of the cobalt ferrite nanoparticles produced by our solvothermal method is close to the results published by Ma et al. (Ms: 70 emu/g)[45]. In the aforementioned work, cobalt ferrite was produced using a solvothermal method similar to the one we applied except that they used hexamethylene tetramine (HMTA) and glycol. For $CoFe_2O_4$particles produced by other methods (co-precipitation and thermal decomposition), Ms values of 33 and 57 emu/g were measured by Aslibeiki et al. and Li et al[46,47]. In case of nickel ferrite, solvothermal synthesis was used to achieve a value of 82.3 emu/g Ms by Wang et al., which exceeds the 57 emu/g measured in our case[48]. Using other synthesis methods, such as co-precipitation, or sol–gel auto-combustion saturation magnetization values between 51 and 67 emu/g were also achieved[43,49].

We determined the specific surface area of the ferrite samples also using the BET method. The cobalt ferrite sample had the largest specific surface area (130.8 m^2/g), while a significantly smaller value was measured for the nickel ferrite (39.3 m^2/g).

Characterization of the silver contained core-shell structured magnetic nanoparticles

TEM images of the $Ag/CoFe_2O_4$ and $Ag/NiFe_2O_4$ MNPs clearly show their core-shell structure in which the silver core is shown with dark contrast (Fig. 6A and B). The shell (with brighter contrast) builds up from ferrite crystallites with small diameter (d: 5–10 nm), which provide efficient magnetic separability. The samples contain a very small number of particles with a fiber morphology, up to 4 micrometers in length (Fig. 6B). Average size of spherical nanoparticles is 276 ± 70 nm ($Ag/CoFe_2O_4$) and 337 ± 109 nm ($Ag/NiFe_2O_4$) (Fig. 6C).

To compare the size distribution of samples containing silver with their counterparts without silver, a size analysis was performed. Larger particle diameters were observed for the core-shell nanoparticles than for the silver-free ferrites (Table 1). This is not only reflected in the average sizes, but also in a size distribution. For

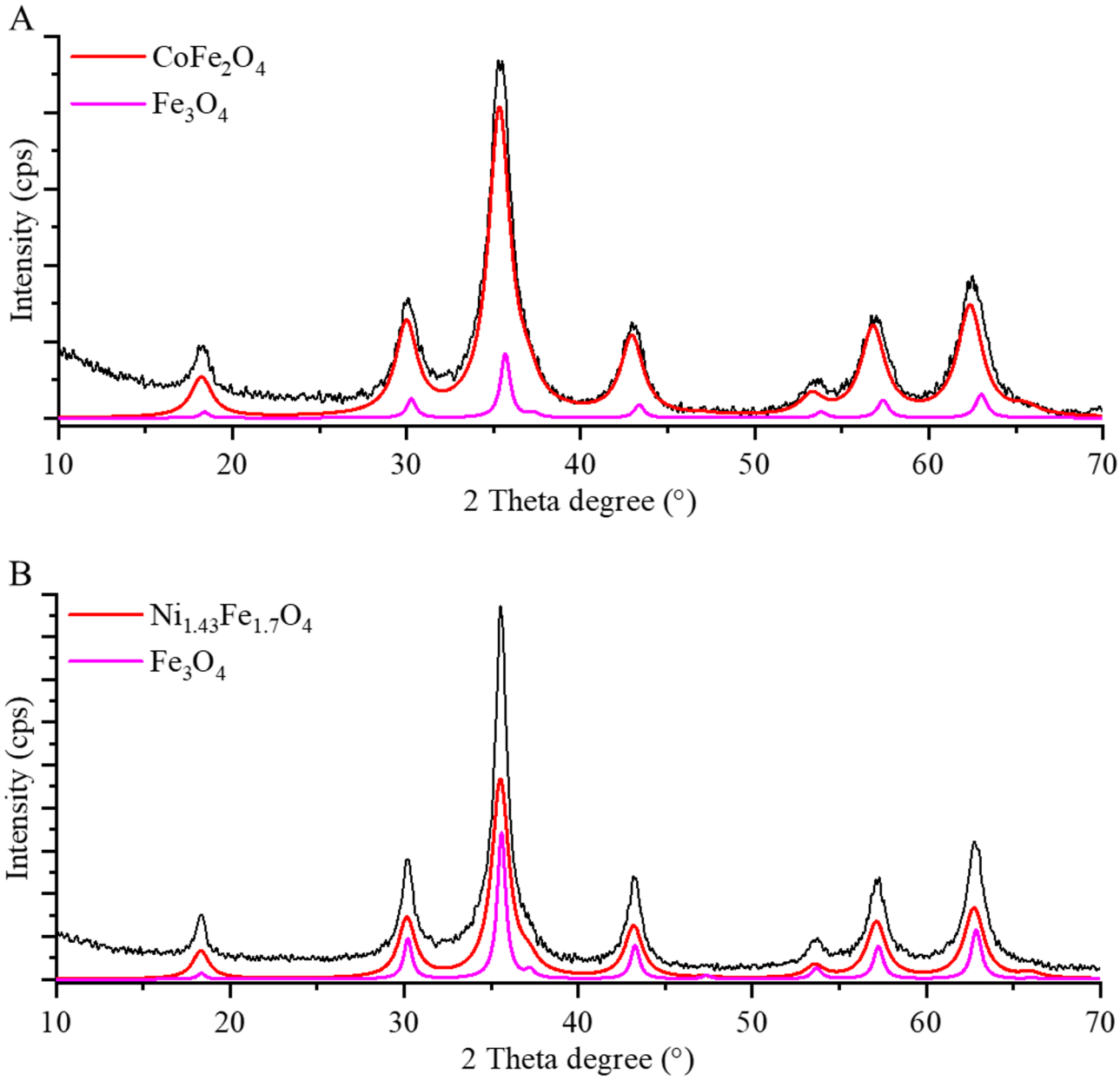

Fig. 4. Rietveld refined XRD patterns of the amine-functionalized $CoFe_2O_4$ (**A**) and $NiFe_2O_4$ (**B**) particles.

$NiFe_2O_4$, 95% of the particles ranged between 152 and 356 nm, whereas in the silver-containing samples, the size range broadened to 111–482 nm. A similar trend was observed for cobalt ferrite samples (Table 1).

In the HAADF images of the amine-functionalized Ag/$CoFe_2O_4$ and Ag/$NiFe_2O_4$ samples, silver particles appear with bright contrast (Fig. 7A and B). These particles are located inside the cobalt ferrite and nickel ferrite spheres as larger inclusions, clearly visible in both the HAADF and elemental maps (Fig. 7A and B). The reduction of silver ions (in a basic medium) by the reducing agent ethylene glycol (EG) resulted in the formation of larger particles. Cobalt and nickel ferrite crystals subsequently began to cluster on their surfaces, leading to development of the core-shell structures observed in the TEM images. This is supported by elemental mapping, which shows that silver is present only in the cores of spherical aggregates, while the shell contains only the elements characteristic of ferrite. Furthermore, in the Ag/$NiFe_2O_4$ sample, silver nanofibers coated with a nickel ferrite layer are also observed (Fig. 7B).

XRD measurements were also performed on the core-shell particles to confirm the presence of elemental silver. In addition to the ferrite and magnetite phases, diffraction peaks corresponding to elemental silver were observed in both samples at two theta angles of 38.1° (111), 44.3° (200) and 64.4° (302) (PDF 04–0783) (Fig. 8A and B). The silver contents of the samples were 25.1 wt% in Ag/$CoFe_2O_4$ and 19.2 wt% in Ag/$NiFe_2O_4$. The magnetite and cobalt ferrite content were 29.3 wt% and 44.2 wt%, respectively. The average particle diameters were 25 ± 5 nm for magnetite and 13 ± 2 nm for spinel.

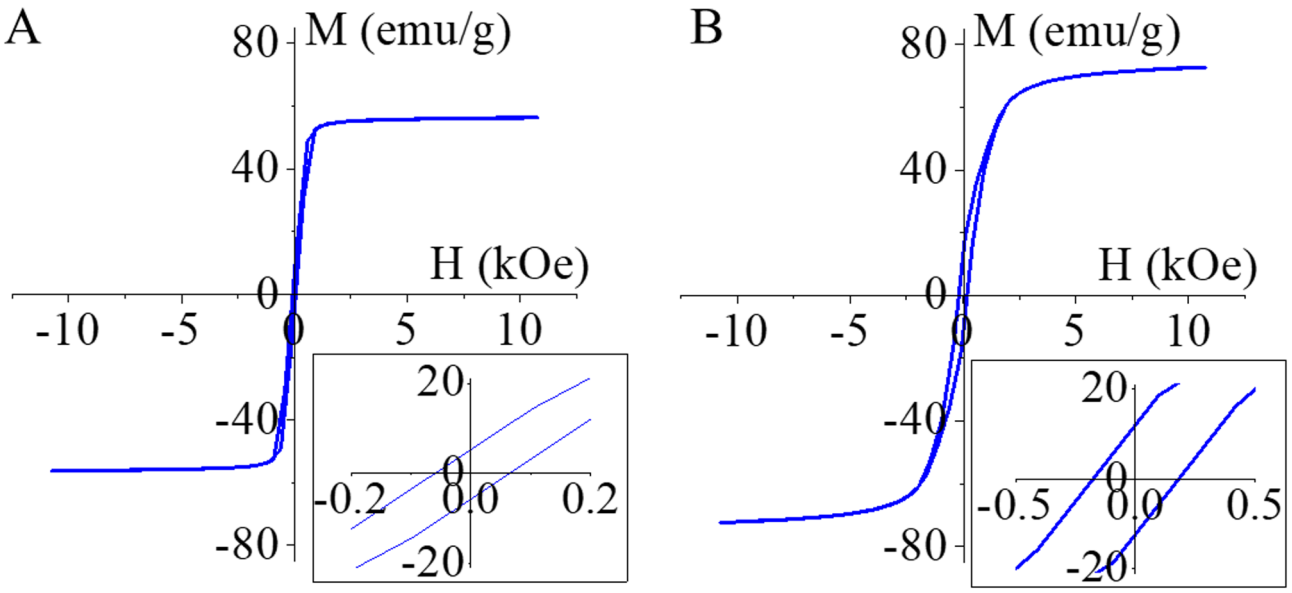

Fig. 5. VSM curve of the amine-functionalized $NiFe_2O_4$ (**A**) and $CoFe_2O_4$ (**B**) samples.

Furthermore, in the $Ag/CoFe_2O_4$ sample, reflections appeared at 44.3 ° and 51.6 ° two theta angles, indicating the formation of a cobalt-silver alloy phase in amount of 1.4 wt%. The calculated particle size was 15 ± 4 nm.

In the $Ag/NiFe_2O_4$ sample, both stoichiometric ($NiFe_2O_4$, 27.5 wt%) and non-stoichiometric ($Ni_{1.43}Fe_{1.7}O_4$, 26.6 wt%) nickel spinel phases were present, the average particle sizes of 8 ± 2 nm and 25 ± 7 nm, respectively. The sample also contained 26.3 wt% magnetite, present as nanoparticles with an average diameter of 28 ± 6 nm. In addition to spinel phases and magnetite, a diffraction peak at 44.3° two theta degree, corresponding to the (200) planes of silver–nickel alloy, was observed in the Rietveld-refined diffractogram of the $Ag/NiFe_2O_4$[50]. Its amount in the sample was 0.4 wt%, with an average particle size of 25 ± 5 nm.

The surfaces functional groups of the nanoparticles were identified using FTIR spectroscopy. The FTIR spectra of the amine-functionalized ferrite nanoparticles showed two characteristic bands: one between 500 and 600 cm^{-1} corresponding to the tetrahedral complexes, and another between 400 cm^{-1} and 450 cm^{-}, which belongs to the octahedral complexes in the spinel structure (Fig. 9A)[51,52]. An absorption band at 598 cm^{-1} corresponds to Fe^{3+}– O^{2-} vibration at A-site of the spinel sublattice. The absorption band at 430 cm^{-1} is attributed to trivalent metal-oxygen vibrations at the octahedral B-sites[51]. The band at 1052 cm^{-1} corresponds to C-O and C-N stretching vibration in all three ferrite samples[53].

The bands at 1407 cm^{-1} and 1533 cm^{-1} were characteristic for the bending vibrations of hydroxyl groups (from the adsorbed ethylene glycol molecules) and the νC = C stretching of adsorbed organic compounds, respectively. The band at 1630 cm^{-1} indicates the presence of adsorbed water molecules. Absorption bands at 2852 cm^{-1} and 2930 cm^{-1} correspond to the symmetric and asymmetric C–H stretching vibrations, respectively. The N–H stretching vibration overlap with those of the -OH groups, resulting in a broad band in the 3000–3700 cm^{-1} region. Due the amine-functionalization of the magnetic nanoparticles, the protonation of $-NH_2$ groups led to positive Zeta potential values: 5 ± 4 mV for $Ag/CoFe_2O_4$ and 11 ± 5 mV for $Ag/NiFe_2O_4$ MNPs, which promotes electrostatic interactions with negatively charged bacterial surfaces such as *E. coli* (Fig. 9B)[54].

Moreover, the surface functional groups of the magnetic ferrite nanoparticles facilitate easy dispersion in aqueous media (Fig. 9C). Due to their magnetic properties, the particles can be readily redispersed and magnetically separated within 30–40 s (Fig. 9C).

VSM measurements of silver-containing core-shell nanoparticles were also performed. The VSM curve of the $Ag/NiFe_2O_4$ sample showed a hysteresis loop with coercivity 47 Oe and remanent magnetization 2.3 emu/g (Fig. 10A). A saturation magnetization (Ms) of 40 emu/g was recorded for the $Ag/NiFe_2O_4$ sample, which is slightly lower than that of the silver-free nickel ferrite. The $Ag/CoFe_2O_4$ sample exhibited a wider hysteresis loop, with a coercivity of 218 Oe and a remanent magnetization of 8.8 emu/g (Fig. 10B). The Ms value was 34 emu/g, which is less than half of that the silver-free cobalt ferrite particles (73 emu/g). The measured values also confirm the ferromagnetic behavior of the silver-containing samples at room temperature.

Characterization of the antibacterial efficiency of magnetic ferrite nanoparticles

For both model organisms (*Escherichia coli* and *Micrococcus luteus*), magnetic nanoparticle (MNP) dispersions were initially tested at a concentration of 30 mg/mL (as the highest concentration used). Antimicrobial activity was observed only for the silver-containing MNPs, as inhibition zones (areas free of bacterial colonies) appeared only around these dispersions on the agar plates inoculated with the bacterial suspensions, as shown in the representative images below (Fig. 11). The applied model organisms were also tested for susceptibility to standard antibiotics, and the corresponding results are provided in the Supplementary Information (Figure S3 and Table S5).

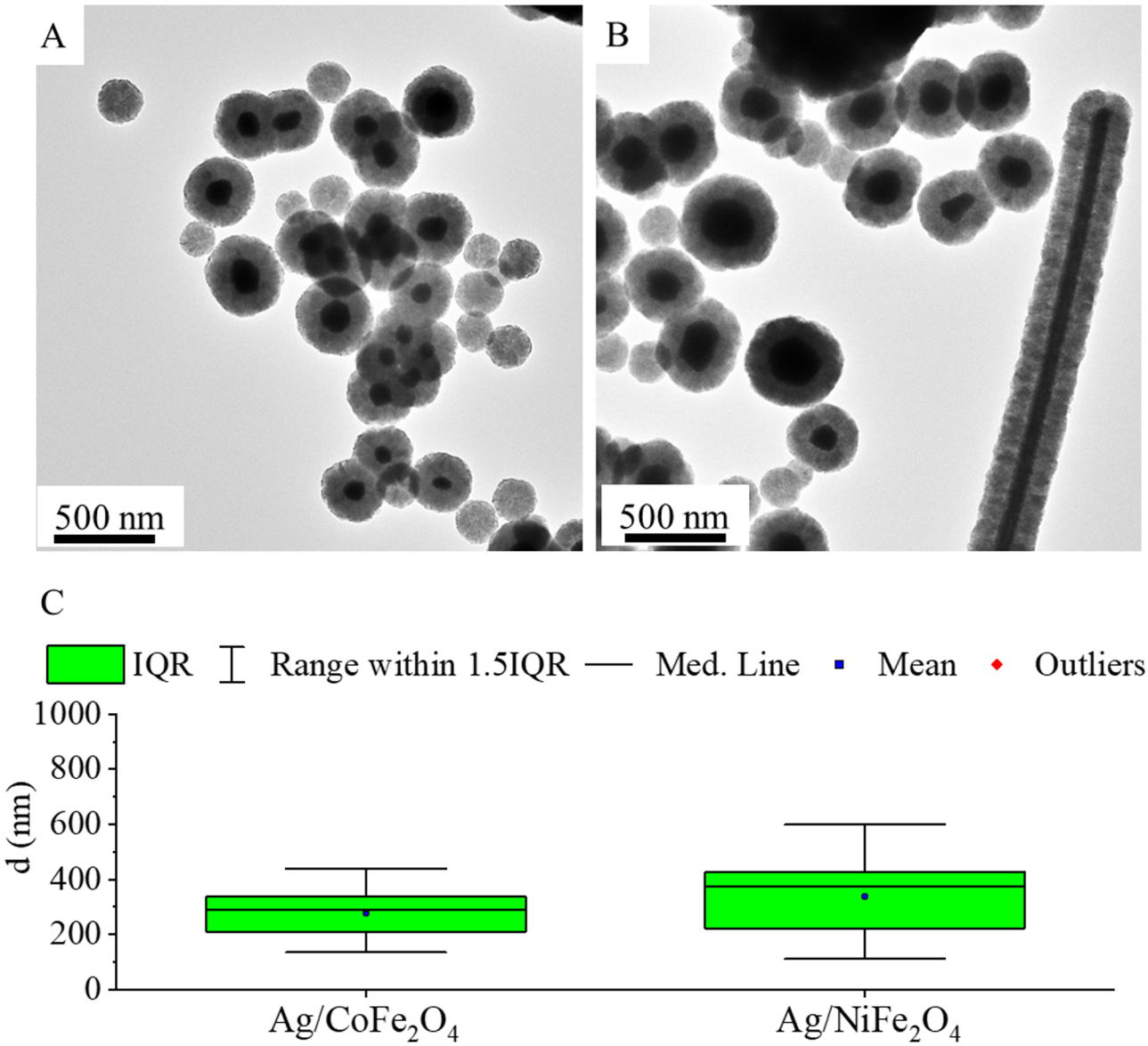

Fig. 6. TEM picture of the amine-functionalized $CoFe_2O_4$ (**A**) and $NiFe_2O_4$ (**B**) samples and their particle size distributions (**C**).

	Mean (nm)	SD (nm)	Min. (nm)	Median (nm)	Max. (nm)	P90 (nm)	P95 (nm)	P99 (nm)
$CoFe_2O_4$	216	34	125	222	274	252	261	272
$NiFe_2O_4$	292	40	152	297	371	336	356	371
$Ag/CoFe_2O_4$	276	70	134	289	438	362	375	413
$Ag/NiFe_2O_4$	337	109	111	372	599	456	482	599

Table 1. Size analysis of the ferrite nanoparticles and their silver contained counterparts.

Consequently, only $Ag/CoFe_2O_4$ and $Ag/NiFe_2O_4$ MNPs were selected for further experiments, in which the minimum inhibitory concentration (MIC) was determined for both *E. coli* and *M. luteus*. Determining the MIC is important because, if particles with antibacterial activity are also intended to be used as adsorbents (e.g., in water purification), it is essential to know the minimum concentration that provides not only adsorption capacity but also antimicrobial activity. Accordingly, the concentration of silver-containing MNP dispersions was gradually reduced. The tested concentrations were as follows: 30 mg/mL, 3 mg/mL, 1 mg/mL, 0.5 mg/mL, and 0.1 mg/mL.

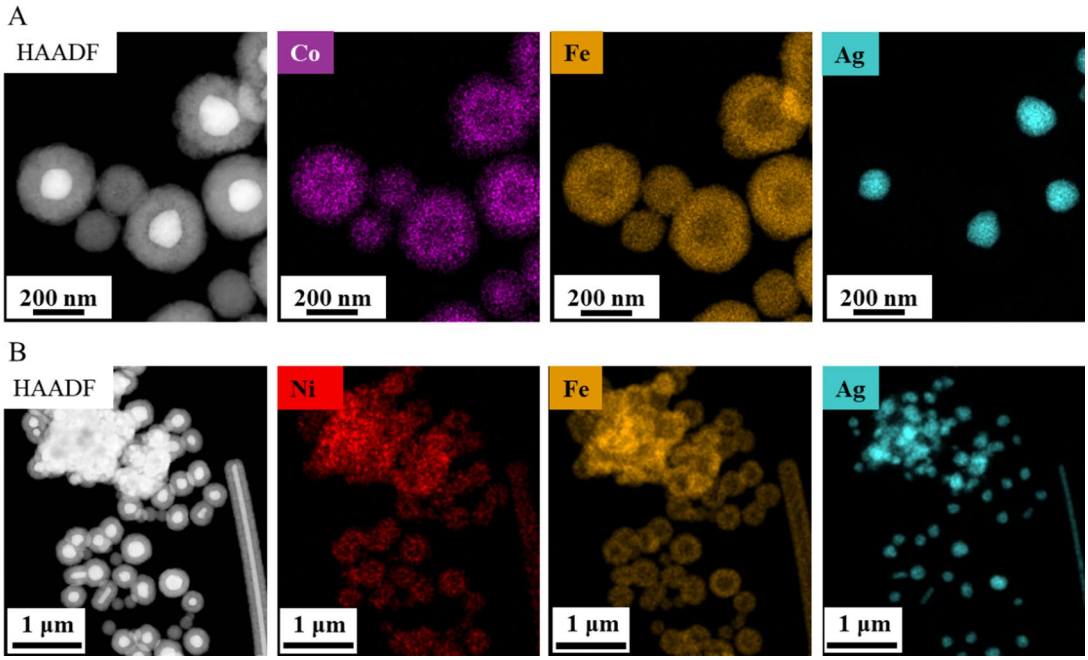

Fig. 7. HAADF pictures and element maps of the amine-functionalized Ag/$CoFe_2O_4$ (**A**) and Ag/$NiFe_2O_4$ MNPs (**B**) Specific surface measurements were also performed using the BET method for silver-containing ferrites. Similar specific surface area values were measured for the silver-containing ferrites with core-shell structure: 39.5 m^2/g (Ag/$CoFe_2O_4$) and 27.5 m^2/g (Ag/$NiFe_2O_4$).

In case of *E. coli*, inhibitory effect was observed even at 0.5 mg/mL MNP concentration, but not at 0.1 mg/mL. Given that no intermediate concentrations between 0.1 and 0.5 mg/mL were tested, the MIC of the silver-containing MNPs for *E. coli* on agar plates was estimated to lie within this range, based on the observed inhibition pattern (Table 2).

Micrococcus luteus, a Gram-positive model organism, was less sensitive to silver-containing particles. In this case, no inhibition zone was observed at 0.1, 0.5 and 1 mg/mL, therefore, 3 mg/mL was identified as the lowest tested concentration that still showed an inhibitory effect. Accordingly, the MIC for *M. luteus* is estimated to be between 1 and 3 mg/mL (Table 2).

The observed difference in the minimum inhibitory concentration (MIC) of silver nanoparticles between *E. coli* (Gram-negative) and *M. luteus* (Gram-positive) in this study aligns well with mechanisms previously described in the literature. The higher sensitivity of *E. coli* (lower MIC) and lower sensitivity of *M. luteus* (higher MIC) are supported by structural and mechanistic differences in the composition of the bacterial cell envelope. The thinner peptidoglycan layer and the lipopolysaccharide-containing outer membrane of Gram-negative bacteria facilitate the adhesion and penetration of AgNPs[55], whereas the thick peptidoglycan wall of Gram-positive cells inhibits these processes[56]. Additionally, the reactive oxygen species (ROS) generated by AgNPs, along with their intracellular damaging effects (e.g., DNA damage, enzyme inhibition), result in a greater degree of inhibition in Gram negative than in Gram positive bacteria[57,58]. Therefore, the difference in MIC values can be well explained by the bacterial cell wall structure and the bactericidal mechanism of the nanoparticles.

Results of adsorption tests

After testing the antibacterial activity of the two types of the MNPs on agar plates, we selected the concentrations used in those assays (specifically the lowest inhibitory and the highest non-inhibitory (sub-inhibitory) concentrations) for subsequent adsorption experiments. Our aim was to evaluate whether these concentrations, determined from plate-based antibacterial tests, could also serve effectively as adsorbent doses in liquid bacterial suspensions.

In first adsorption test, a high concentration of MNPs (30.0 mg/mL) were applied for both model organism. This resulted in complete removal of bacterial cells from the supernatant, and no colony formation was observed when the pellet (containing MNPs and adsorbed cells) was plated on agar, indicating both strong adsorption and bactericidal activity due to the presence of silver (Tables 3 and 4).

Subsequently, the MNP concentration was reduced to 0.5 and 0.1 mg/mL for *E. coli* and to 3.0 and 1.0 mg/mL for *M. luteus*, based on the previously determined inhibitory and sub-inhibitory concentrations (Table 2). As summarized in the Tables 3 and 4, the lowest inhibitory concentration for *M. luteus* (3.0 mg/mL of Ag/$CoFe_2O_4$ or Ag/$NiFe_2O_4$) was highly effective as an adsorbent, leading to complete removal of cells from the supernatant and the absence of viable colonies in the pellet. Notably, even the sub-inhibitory concentration (1.0 mg/mL) showed similar performance, suggesting that concentrations below the MIC (though non-inhibitory on agar) can still exert strong antibacterial and adsorptive effects in liquid media.

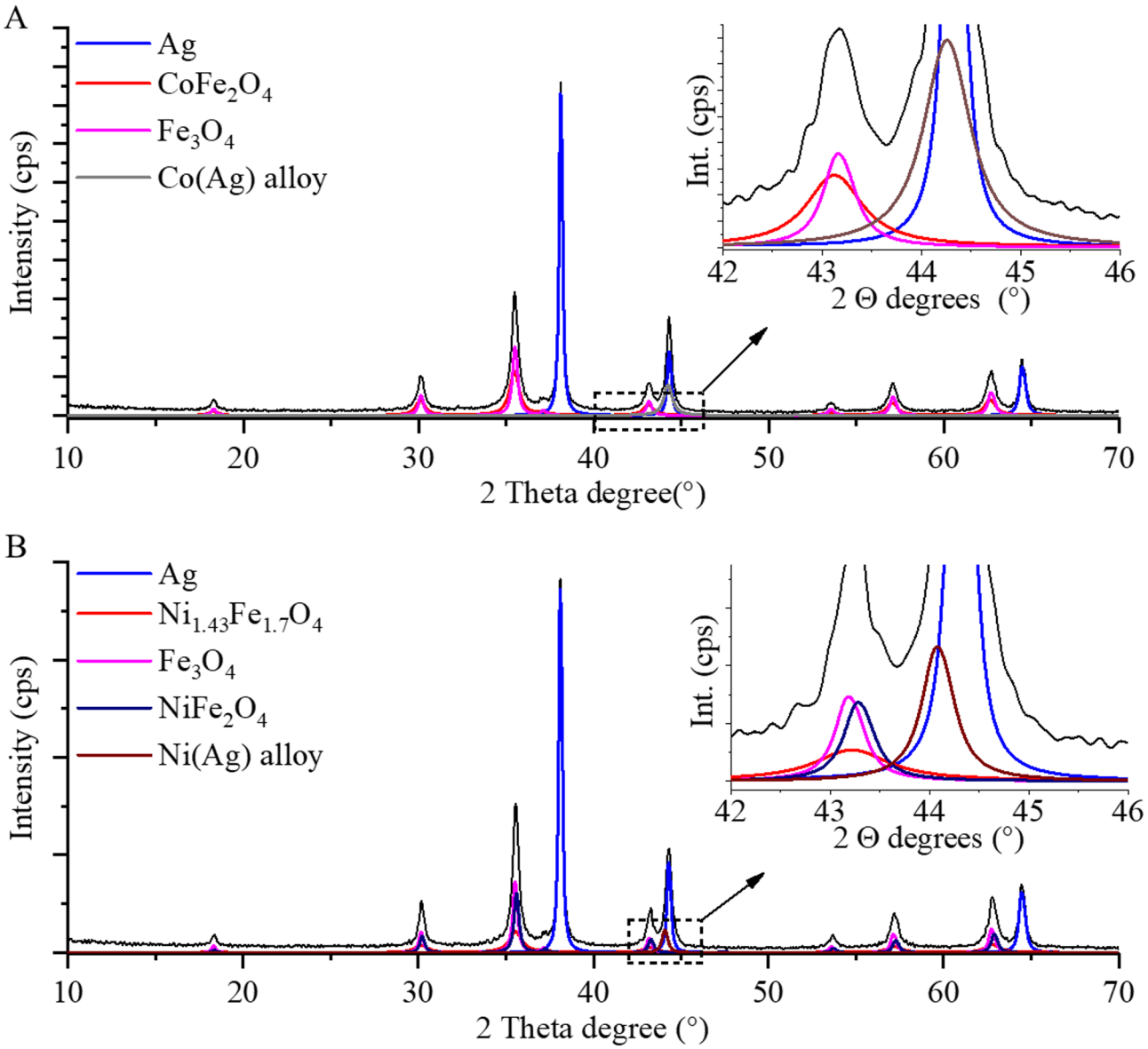

Fig. 8. Rietveld refined XRD patterns of the amine-functionalized Ag/$CoFe_2O_4$ (**A**) and Ag/$NiFe_2O_4$ (**B**) samples.

The observed differences of the effective inhibitory concentration of the Ag-containing MNPs on agar plates and in broth microdilution may be explained by the fact that, in a well-mixed liquid system, even lower silver concentrations can exhibit antibacterial effects. In contrast, on solid surface, antimicrobial activity is typically localized and depends on the diffusion range of the silver ions (i.e., producing zone of inhibition)[59].

For *E. coli*, the MIC concentration of Ag/$CoFe_2O_4$ (0.5 mg/mL) did not result in complete bacterial removal, although the cell count in the supernatant was significantly reduced (below detection limit). Similarly, the sub-inhibitory concentration (0.1 mg/mL) showed > 95% efficiency but did not achieve full antibacterial or adsorptive effect. Therefore, to further assess performance of Ag/$CoFe_2O_4$ MNP, an additional concentration of 1.0 mg/mL (2×MIC, based on the value obtained from agar plate tests) was examined. At this level, complete bacterial removal was achieved in the supernatant, and no colony formation was observed from the pellet, confirming that doubling the MIC concentration ensured both full adsorption and antibacterial activity for *E. coli* when using Ag/$CoFe_2O_4$ MNPs (Table 3).

In parallel, experiments with Ag/$NiFe_2O_4$ nanoparticles at the lowest inhibitory concentration (0.5 mg/ml) and at a sub-inhibitory concentration (0.1 mg/mL) also resulted in the complete elimination of detectable *E. coli* cells from both the supernatant and the pellet phase (Table 4).

These findings highlight the complex interplay between several MNP characteristics (including dispersion stability, magnetic saturation, particle size) and bacterial adsorption efficiency. Ag-functionalized $CoFe_2O_4$ nanoparticles exhibited high bacterial adsorption efficiency, achieving over 95% removal even at concentrations as low as 0.1 mg/mL. This performance is likely associated with their slightly lower dispersion stability compared

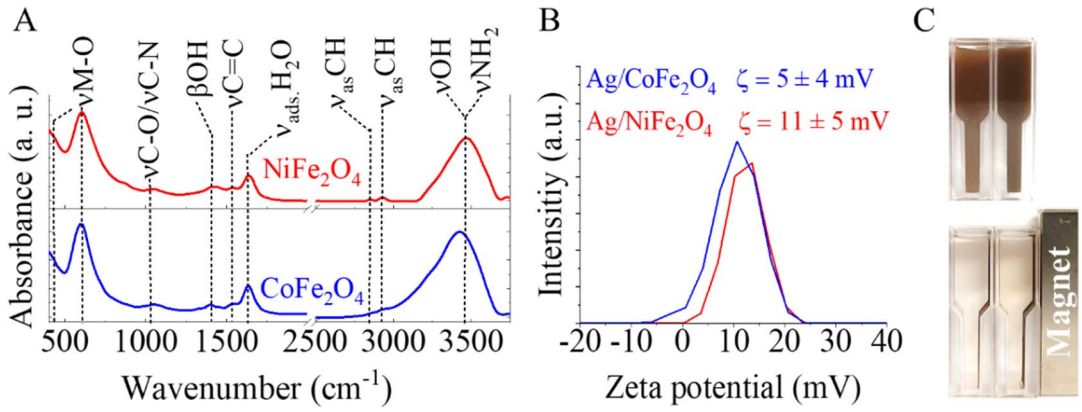

Fig. 9. FTIR spectrum (**A**), zeta potential distribution (**B**) and magnetic separation (**C**) of the amine-functionalized $Ag/CoFe_2O_4$ and $Ag/NiFe_2O_4$ MNPs.

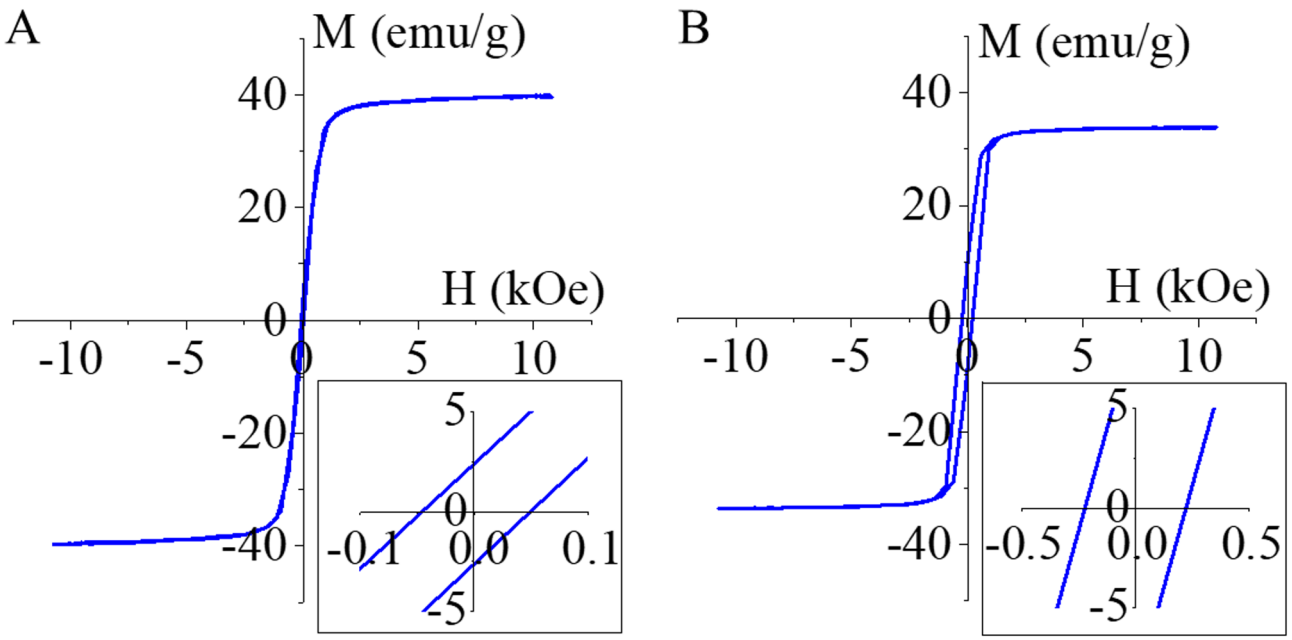

Fig. 10. VSM curve of the amine-functionalized $Ag/NiFe_2O_4$ (**A**) and $Ag/CoFe_2O_4$ (**B**) samples.

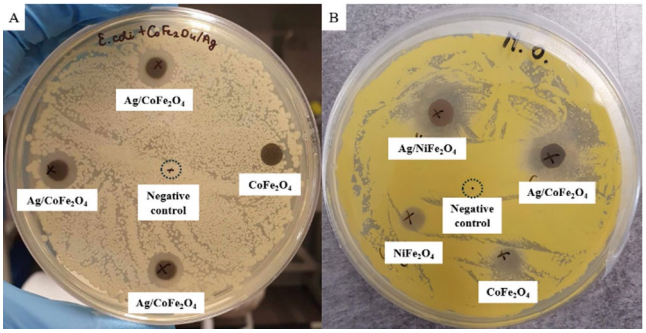

Fig. 11. Representative inhibition zone assays with *E. coli* (**A**) and *M. luteus* (**B**). Amin-functionalized magnetic nanoparticles (30 mg/mL) were tested on LB agar; clear zones are visible only around the silver-containing MNPs. Sterile LB served as negative control.

Type of microorganism	E. coli (Gram-negative)		M. luteus (Gram-positive)	
Type of magnetic nanoparticle	Applied concentration [mg/mL]	Diameter of the inhibition zone [mm]	Applied concentration [mg/mL]	Diameter of the inhibition zone [mm]
$Ag/CoFe_2O_4$	30.0	11.6	30.0	11.5
	3.0	8.9	3.0	5.7
	1.0	6.7	1.0	0
	0.5	6.7	0.5	0
	0.1	0	0.1	0
$Ag/NiFe_2O_4$	30.0	10.3	30.0	12.2
	3.0	8.6	3.0	6.2
	1.0	6.7	1.0	0
	0.5	7.2	0.5	0
	0.1	0	0.1	0

Table 2. Antibacterial testing results of $Ag/CoFe_2O_4$ and $Ag/NiFe_2O_4$ nanoparticles. The MIC values and the corresponding Inhibition zone diameters are highlighted in grey.

to the silver-functionalized $NiFe_2O_4$ nanoparticles, as reflected by their zeta potential (+5 mV for $Ag/CoFe_2O_4$ vs. +11 mV for $Ag/NiFe_2O_4$). At such low concentrations (0.1–0.5 mg/mL), completely homogeneous dispersion of the $Ag/CoFe_2O_4$ nanoparticles in the suspension may not have been fully achieved. Partial sedimentation could have occurred, preventing some particles from contributing to adsorption. Nevertheless, the remaining dispersed particles, along with the silver ions released, were still effective enough to eliminate over 95% of the bacteria. This is particularly noteworthy given the moderate magnetic saturation (34 emu/g) and relatively large average particle size (276 nm). While larger particle sizes generally reduce surface area and may promote aggregation, the observed results suggest that the nanoparticles maintained sufficient dispersion and interaction with bacterial cells, especially at concentrations of 1.0 mg/mL and above. Additionally, their magnetic properties were adequate for post-treatment separation using an external magnetic field.

The efficient adsorption and antibacterial performance of the silver-containing magnetic nanoparticles can be attributed to their surface charge and morphology. Literature data confirm that positively charged nanoparticles are more effective adsorbents due to electrostatic interactions with the negatively charged bacterial cell membranes[60–63]. Our results align with this understanding, as the tested particles exhibited positive surface charges and achieved near-total bacterial removal.

Furthermore, the spherical morphology of the nanoparticles may have contributed to their antibacterial efficacy. Spherical silver nanoparticles are known to release silver ions more efficiently than other shapes (e.g., triangular plates or disks), enhancing their antimicrobial activity through more effective disruption of bacterial membranes and interference with essential cellular functions[64]. Both nanoparticle size and surface characteristics influence the release rate of silver ions. While size affects the contact area and interaction with the surrounding medium, surface charge and composition impact colloidal stability and dissolution behavior[65].

Overall, the nearly complete antibacterial and adsorption efficiency observed, even at very low concentrations, can be attributed to the favorable combination of positive surface charge, spherical shape, and silver content. These properties are consistent with existing knowledge on nanoparticle–bacteria interactions.

In all tested concentrations, the silver component of both $Ag/CoFe_2O_4$ and $Ag/NiFe_2O_4$- nanoparticles contributed significantly to bacterial growth inhibition. These results demonstrate that $Ag/CoFe_2O_4$ and $Ag/NiFe_2O_4$ are highly promising candidates for magnetic-assisted bacterial removal in aqueous systems.

Time-kill kinetic assay

To further evaluate the bactericidal activity of the silver-containing MNPs, time-kill kinetic assays were performed. For these experiments, we selected MNP concentrations that had previously demonstrated consistent antibacterial and adsorptive efficacy both on agar plates and in liquid suspension. Specifically, 1.0 mg/mL was applied for *E. coli* and 3.0 mg/mL for *M. luteus*, using both $Ag/CoFe_2O_4$ and $Ag/NiFe_2O_4$ nanoparticles. These concentrations were chosen to ensure reliable antimicrobial performance, as they had already shown complete bacterial removal in prior endpoint assays.

As shown in Fig. 12, no viable bacterial colonies were detected from either the supernatant or the pellet at any time point. The MNPs exerted their antibacterial effect within the first 10 min of contact, leading to complete elimination of bacterial cells from the system. These findings confirm the rapid and potent bactericidal action of the silver-functionalized MNPs under the tested conditions. The corresponding agar plate images related to the data shown in Fig. 12 are provided in the Supplementary Information as Table S1-S4.

Conclusions

We successfully synthesized core-shell structured particles with average diameters of 276 ± 70 nm ($Ag/CoFe_2O_4$) and 337 ± 109 nm ($Ag/NiFe_2O_4$) using a polyol-based solvothermal synthesis method. These particles showed good adsorption onto the cell walls of pathogenic microorganisms such as *Escherichia coli* and *Micrococcus*

Type of microor-ganisms	Applied MNP concentration in solution [mg/mL]	C_i [cfu/mL]	C_{ua} [cfu/mL]	Adsorption efficiency (E%)	C_{ads} [cfu/mL]	Representative agar plate images
E. coli(Gram-negative)	**30.0** (highest tested concentration)	$1.5 \pm 0.4 \times 10^8$	0	**100**	0	
	1.0 (2×MIC)	$5.4 \pm 1.5 \times 10^8$	0	**100**	0	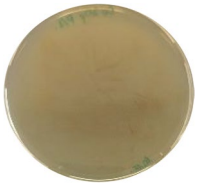
	0.5 (lowest inhibitory concentration on agar plate)	$7.2 \pm 1.1 \times 10^8$	bdl.	**>95%**	bdl.	
	0.1 (sub-inhibitory concentration on agar plate)	$1.2 \pm 0.3 \times 10^8$	bdl.	**>95%**	bdl.	
M. luteus(Gram-positive)	**30.0** (highest tested concentration)	$3.2 \pm 0.6 \times 10^8$	0	**100**	0	
	3.0 (lowest inhibitory concentration on agar plate)	$2.7 \pm 0.6 \times 10^8$	0	**100**	0	
	1.0 (sub-inhibitory concentration on agar plate)	$2.7 \pm 0.6 \times 10^8$	0	**100**	0	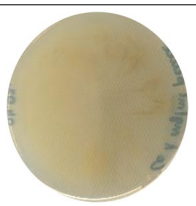

Table 3. Adsorption results of $Ag/CoFe_2O_4$ nanoparticles (bdl: below detection limit). Adsorption efficiency was calculated as, where is the initial viable cell concentration and is the unadsorbed cell concentration. The concentration of adsorbed viable bacteria is denoted as. The last column presents representative agar plate images to visually support the quantitative data shown.

luteus. Adsorption experiments demonstrated that both types of silver-containing nanoparticles achieved near-complete (approximately 100%) bacterial removal efficiency for both bacterial strains, even at concentrations as low as 0.1 mg/mL. The high adsorption activity of these nanoparticles can be attributed to a positive surface charge (their electrokinetic potentials are 5 ± 4 and 11 ± 5 mV) that facilitates electrostatic interactions with the negatively charged bacterial membranes. Moreover, their high Ms values (73 emu/g for $Ag/CoFe_2O_4$ and

Type of microor-ganisms	Applied MNP concentration in solution [mg/mL]	C_i [cfu/mL]	C_{ua} [cfu/mL]	Adsorption efficiency (E%)	C_{ads} [cfu/mL]	Representative agar plate images
E. coli **(Gram-negative)**	**30.0** (highest tested concentration)	$5.6 \pm 0.4 \times 10^8$	0	**100**	0	
	0.5 (lowest inhibitory concentration on agar plate)	$5.2 \pm 0.2 \times 10^8$	0	**100**	0	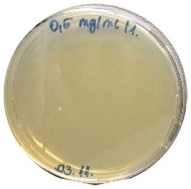
	0.1 (sub-inhibitory concentration on agar plate)	$4.8 \pm 0.3 \times 10^8$	0	**100**	0	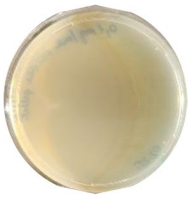
M. luteus **(Gram-positive)**	**30.0** (highest tested concentration)	$3{,}2 \pm 0{,}6 \times 10^8$	0	**100**	0	
	3.0 (lowest inhibitory concentration on agar plate)	$2.7 \pm 0.6 \times 10^8$	0	**100**	0	
	1.0 (sub-inhibitory concentration on agar plate)	$2.7 \pm 0.6 \times 10^8$	0	**100**	0	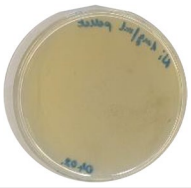

Table 4. Adsorption results of $Ag/NiFe_2O_4$ nanoparticles adsorption efficiency was calculated using the following equation:, where is the initial viable cell concentration and is the unadsorbed cell concentration. The concentration of adsorbed viable bacteria is denoted as. The last column presents representative agar plate images to visually support the quantitative data shown.

57 emu/g for $Ag/NiFe_2O_4$) enables rapid and efficient separation from aqueus media via magnetic separation. This dual functionality allows for both the removal and inactivation of microbial contaminants, reducing the infectivity of magnetically recovered sewage sludge. For *E. coli*, significant antibacterial activity was observed at concentrations as low as 0.5 mg/mL, whereas for *M. luteus*, inhibition was only evident at or above 3 mg/mL. This discrepancy is attributed to fundamental differences in the cell wall structure of Gram-negative and Gram-positive bacteria. Viable cell counts in the supernatant dropped below the detection limit, and no colony growth was observed from the pellet when plated on agar, further confirming bactericidal activity. To further validate these findings, time-kill kinetic assays were performed using concentrations that had previously demonstrated complete antibacterial and adsorptive efficacy in both agar and liquid-phase tests. Specifically, 1.0 mg/mL was applied for *E. coli* and 3.0 mg/mL for *M. luteus*, using both $Ag/CoFe_2O_4$ and $Ag/NiFe_2O_4$ nanoparticles. The results confirmed that the silver-functionalized MNPs exerted their bactericidal effect within the first 10 min of contact, with no viable cells detected at any time point. Notably, in the *E. coli*–$Ag/CoFe_2O_4$ system, the 1.0 mg/

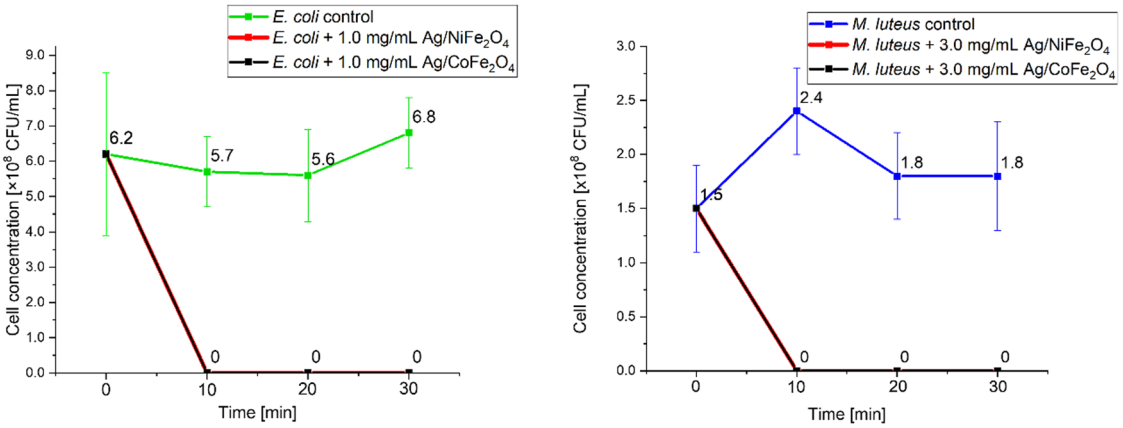

Fig. 12. Time–kill kinetic assay results for *E. coli* and *M. luteus*. Adsorbent-free bacterial suspension served as control.

	$Ag(NO_3)$	$Ni(NO_3)_2{\cdot}6\,H_2O$	$Co(NO_3)_2{\cdot}6\,H_2O$	$Fe(NO_3)_3{\cdot}9H_2O$
$NiFe_2O_4$	-	1.75 g (6 mmol)	-	4.85 g (12 mmol)
$CoFe_2O_4$	-	-	1.75 g (6 mmol)	4.85 g (12 mmol)
$Ag/NiFe_2O_4$	0.51 g (3 mmol)	1.75 g (6 mmol)	-	4.85 g (12 mmol)
$Ag/CoFe_2O_4$	0.51 g (3 mmol)	-	1.75 g (6 mmol)	4.85 g (12 mmol)

Table 5. Amounts of the respective transition metal nitrates dissolved in the reaction media for the synthesis of the NH_2-functionalized ferrite nanoparticles.

mL concentration – corresponding to 2× the MIC determined on agar – was required to achieve complete bacterial removal in liquid suspension, highlighting the importance of medium-dependent optimization.

Collectively, these findings suggest that amine-functionalized $Ag/NiFe_2O_4$ and $Ag/CoFe_2O_4$ nanoparticles exhibit potent antibacterial and bacterial adsorption capabilities at low concentrations, with rapid and effective performance in both solid and liquid environments. These properties make them highly promising candidates for magnetic-assisted water purification applications.

Materials and methods

Materials

The silver contained, amine-functionalized ferrite nanoparticles were made from nickel(II) nitrate hexahydrate, $Ni(NO_3)_2 \cdot 6\,H_2O$, MW:290.79 g/mol (Thermo Fisher GmbH, D-76870 Kandel, Germany); cobalt(II) nitrate hexahydrate, $Co(NO_3)_2\,6\,H_2O$, MW: 291.03 g/mol and iron(III) nitrate nonahydrate, $Fe(NO_3)_3{\cdot}9H_2O$, MW: 404.00 g/mol (VWR Int. LtD., B-3001 Leuven, Belgium) respectively. As dispersion medium ethylene glycol, $HOCH_2CH_2OH$, (VWR Int. Ltd., F-94126 Fontenay-sous-Bois, France) was applied. For coprecipitation and functionalization of the ferrites, monoethanolamine (MEA), $NH_2CH_2CH_2OH$ (Merck KGaA, D-64271 Darmstadt, Germany) and sodium acetate, CH_3COONa (ThermoFisher GmbH, D-76870 Kandel, Germany) were used. Decomposition of silver nanoparticles was carried from silver nitrate; $Ag(NO)_3$, MW: 169.87 g/mol (ThermoFisher GmbH, D-76870 Kandel, Germany). For the LB-solution, physiological saline solution and agar-plates tryptone, yeast extract (Neogen Culture Media, Lansing, MI, USA), sodium-chloride and bacteriological agar (VWR International, Leuven, Belgium) was used.

Methods

Preparation of the amine-functionalized, silver contained, magnetic spinel nanoparticles

Amine-functionalized ferrite magnetic particles were synthesized according to a solvothermal method. Iron(III) nitrate nonahydrate and the nitrate salt of the respective transition metal (Co or Ni) were dissolved (Table 5) in 100 mL ethylene glycol. Sodium acetate 2.46 g (30 mmol) was dissolved in the ethylene-glycol based solution of the metal precursors under continuous stirring, followed by the addition of 20 mL ethanol amine. The solution was transferred in Teflon lined hydrothermal autoclave (100 mL), and heated at 200 °C for 12 h. After cooling, the solid phase was separated from the dispersion using magnet and washed several times with distilled water. Finally, the ferrite was rinsed with anhydrous ethanol and dispersed in distilled water. The synthesis of the silver-containing ferrite samples differed from the above-mentioned method in that 0.51 g (3 mmol) of silver nitrate was dissolved in the reaction mixture prior to hydrothermal treatment. In antibacterial tests, silver-free nickel ferrite and cobalt ferrite were used as controls, thus these materials were synthetized also.

The formation of transitional metal ferrite nanoparticles is assisted by the transformation of monoethanol amine (MEA), because the presence of M(II) (whereas M = Co^{2+} or Ni^{2+}) ions reduces the thermal decomposition

temperature of MEA[66] and ammonia is released. Furthermore, Rochell has shown that the presence of Fe(III) ions promotes the oxidative degradation of MEA, during this process aminium radical is formed which is deprotonated to imine radical which is further degraded to ammonia and aldehyde (hydroxyacetaldehyde) via imine[67]. The alkaline conditions lead to the formation of $Fe(OH)_3$ and $M(OH)_2$, which can be transformed into $CoFe_2O_4$ and $NiFe_2O_4$ through dehydration.

$$NH_2\,CH_2CH_2OH \xrightarrow{Fe^{3+}\,and\,-H^+} H_2N^* = CH - CH_2 - OH + H_2O \xrightarrow{Fe^{3+}\,-H^+} HOCH_2CHO + NH_3$$

$$NH_3 + H_2O \rightarrow NH_4^+ + OH^-$$

$$Fe^{3+} + 3\,OH^- \rightarrow Fe(OH)_3$$

$$M^{2+} + 2\,OH^- \rightarrow M(OH)_2$$

$$M(OH)_2 + 2\,Fe(OH)_3 \rightarrow MFe_2O_4 + 4\,H_2O$$

Characterization techniques

The particle-size, morphology and crystalline phases of the ferrite particles were determined using high-resolution transmission electron microscopy (HRTEM). For the HRTEM measurements, Talos F200X G2 electron microscope with field emission electron gun, X-FEG (accelerating voltage 20–200 kV) was used. For the imaging and selected area electron diffraction (SAED) measurements, SmartCam digital search camera (Ceta 16 Mpixel, 4k x 4k CMOS camera) was used with a high-angle annular dark-field (HAADF) detector. During the HRTEM examination, the aquaeous dispersion of ferrite was dropped onto 300 mesh copper grids (Ted Pella Inc., 4595 Redding, CA 96003, USA). X-ray diffraction (XRD) measurements were performed to identify and quantify the ferrite samples using Bruker Discovery diffractometer (Cu-Kα source, 40 kV and 40 mA) in parallel beam geometry (Göbel mirror) with Vantec detector, using Powder Diffraction Files (PDFs). The average crystal size of ferrite domains was calculated using the mean column length method, calibrated based on the full width of half maximum (FWHM) and the width of the Lorentzian component of the fitted profiles (for the evaluation, TOPAS 4 software was applied). The ferrite samples were examined with Fourier transform infrared spectroscopy (FTIR) by a Bruker Vertex 70 spectroscope in transmission mode for identified their surface functional groups. For the FTIR measurements 15 mg of the sample was pelletized with 250 mg spectroscopic grade KBr. The magnetic characterization of ferrite nanoparticles was performed using custom-built vibrating-sample magnetometer system, developed at the University of Debrecen and based on a water-cooled Weiss-type electromagnet. The powder samples were pelletized for the measurements with a typical mass of 20 mg. The magnetization (M) was measured as a function of the magnetic field (H) up to a 10,000 Oe field strength at room temperature. The electrokinetic potential of the magnetic particles was determined from electrophoretic mobility using laser Doppler electrophoresis with an Anton Paar Litesizer DLS 500 instrument (Anton Paar GmbH, Graz, Austria). The specific surface area (SSA) measurements of the samples were carried out by nitrogen adsorption-desorption method at 77 K. For this, the Micromeritics ASAP 2020 equipment was used, and the evaluation was carried based on the Brauner-Emmett-Teller (BET) method.

Preparation of LB broth, LB agar plates, and physiological saline solution

To prepare the LB (Luria-Bertani) broth, the solid components (10 g tryptone, 5 g yeast extract, 10 g sodium chloride) were dissolved in 1000 mL of ultrapure water using a magnetic stirrer. Then the LB solution was distributed into 100 mL Erlenmeyer flasks, 35 mL per flask, and sterilized with cotton plugs in an autoclave (121 °C, 15 min, 103–117 kPa).

For the LB agar plates, 15 g of bacteriological agar was added to 1000 mL of LB broth, then sterilized in glass bottles. The hot LB agar was cooled to 50 °C in water bath, and the mixture was dosed into sterile Petri dishes with 90 mm diameter and allowed to solidify. These plates can be stored in a refrigerator at 4 °C for up to one month.

The physiological saline solution was used to create a dispersion of the bacterial cells and magnetic nanoparticles. For the preparation of the saline solution 8.5 g of NaCl was dissolved in 1000 mL of ultrapure water, then sterilized in glass bottles in an autoclave at 121 °C for 15 min.

Antibacterial property testing of magnetic nanoparticles

The antibacterial activity of magnetic nanoparticles was tested against *Micrococcus luteus* (*M. luteus*, Gram-positive) and *Escherichia coli* ATCC 25,922 (*E. coli*, Gram-negative) bacterial strains. Initially, a single bacterial colony was transferred into a flask containing 35 mL of LB culture medium using a sterile inoculum loop. The cultures were incubated under optimal conditions: *Micrococcus* at 30 °C and 160 rpm for 72 h, and *E. coli* at 37 °C and 160 rpm for 24 h, in a shaking incubator.

The optical density (OD) of the bacterial suspension was measured at 600 nm to assess cell concentration, using LB as the blank solution with NanoDrop™ (ThermoFisher Scientific, Waltham, MA, USA). This was necessary in order to determine the cell density, as a higher OD value indicates a greater number of bacterial cells in the suspension. Therefore, OD measurements can be used to infer the initial cell concentration for the tests. To ensure that the antibacterial tests are always performed with uniformly dense bacterial suspensions, the cultures were diluted to an OD of 0.1.

To determine the cell concentration belonging to $OD_{600} = 0.1$, a tenfold serial dilution was prepared, and 3×100 µl of the 10^6 dilution were spread onto LB agar. The resulting colony counts (30–300 colonies/plate) were used for concentration calculations.

For antibacterial testing 100 µl of the 10^2 dilution was spread on LB agar, forming a continuous bacterial layer. MNP dispersions (10 µl) were applied to the surface, with distilled water as a negative control to confirm that the antibacterial effect originates from the nanoparticles and not from the dispersing agent.

Following incubation, a clearing zone appeared on the plate around the antibacterial magnetic nanoparticles, indicating microbial growth inhibition. The size (diameter) of the inhibition zone depended on the concentration of the magnetic nanoparticle dispersion being tested, as more concentrated dispersion produces larger inhibition zone. The minimum inhibitory concentration (MIC) was determined by progressively reducing MNP dispersion concentration to establish the lowest concentration still exhibiting antibacterial activity.

Adsorption tests for bacterial removal

For adsorption experiments, either *Micrococcus luteus* or *Escherichia coli* was incubated overnight under optimal growth conditions (30–37 °C with 160 rpm shaking). The bacterial suspension was adjusted to $OD_{600} = 0.1$ to standardize the initial cell concentration. A tenfold serial dilution was prepared, and 3×100 µl of the 10^6 dilution were plated to determine the initial viable cell concentration (denoted as C_i in cfu/mL).

Magnetic nanoparticles were prepared at an initial concentration of 30 mg/mL using 205 µL of the initial Ag/$NiFe_2O_4$-NH_2 dispersion (146 mg/mL) and 192 µL Ag/$CoFe_2O_4$-NH_2 (156.7 mg/mL). After water removal via magnetic separation, the particles were resuspended in 900 µl sterile physiological saline solution. Then, 100 µl of the 10^5-diluted bacterial suspension was added to this mixture, yielding a final dilution of 10^6 in the MNP dispersion. The prepared dispersion was rotated for 30 min to facilitate even distribution of the bacterial adsorption onto MNPs. Following separation using a magnetic stand, 3×100 µl of the supernatant (containing the unbounded bacterial cells) was plated to determine the unadsorbed cell concentration (C_{ua}). The MNPs were then resuspended in fresh saline, and the adsorbed viable bacteria (C_{ads}) were quantified by plating. This step demonstrated how many of the bound microorganisms survived in the presence of silver-containing MNPs.

Subsequently, the adsorption experiment was repeated using lower MNP concentrations based on prior antibacterial results for *E. coli* and *M. luteus*, respectively. The MIC was determined to be 0.5 mg/mL for *E. coli* and 3 mg/mL for *M. luteus*, as these were the lowest concentrations that exhibited antibacterial activity. In contrast, 0.1 mg/mL had no antibacterial effect on *E. coli*, while 1 mg/mL showed no inhibitory activity against *M. luteus*, with neither concentration producing a clearing zone on agar plates.

Based on these findings, the adsorption tests were conducted using the lowest MNP concentration that still exhibited antibacterial activity (0.5 mg/mL for *E. coli* and 3 mg/mL for *M. luteus*), along with the next lower tested concentration (0.1 mg/mL for *E. coli* and 1 mg/mL for *M. luteus*) to evaluate whether MNP dispersions that showed no antibacterial effect on agar plates could still influence bacterial viability during the adsorption process. This approach allowed for a comparative analysis of bacterial adsorption under conditions with and without detectable antibacterial activity.

Time-kill kinetic assay

Time-kill kinetic measurements were conducted to assess the temporal dynamics of bacterial inactivation by silver-containing MNPs. For each model organism, a concentration previously confirmed to be fully antibacterial and adsorptive was selected: 1.0 mg/mL for *E. coli* and 3.0 mg/mL for *M. luteus*. Bacterial suspensions were added to the respective MNP dispersions and incubated on a rotator mixer at room temperature. Samples were collected from both the supernatant and the pellet fractions after 10, 20, and 30 min of incubation. An adsorbent-free bacterial suspension was used as a control, subjected to identical mixing and sampling conditions. Earlier time points (< 10 min) were not feasible due to technical limitations in parallel sampling. Higher concentrations (e.g., 2×MIC or 4×MIC) were not tested, as previous studies[68,69] have shown that they accelerate cell death, and our setup did not allow for shorter contact time evaluation.

Data availability

Data is available upon request from the corresponding authors.

Received: 1 July 2025; Accepted: 19 December 2025
Published online: 26 December 2025

References

1. Keshri, S. & Biswas, S. Synthesis, physical properties, and biomedical applications of magnetic nanoparticles: a review. *Prog Biomater.* **11**, 347–372 (2022).
2. Li, Z., Zhang, J., Li, X., Guo, X. & Zhang, Z. Preparation and evaluation of multifunctional autofluorescent magnetic Nanoparticle–Based drug delivery systems against mammary cancer. *J. Pharm. Sci.* **107**, 2694–2701 (2018).
3. Ilosvai, Á. M. et al. Development of Polymer-Encapsulated, Amine-Functionalized zinc ferrite nanoparticles as MRI contrast agents. *Int. J. Mol. Sci. 2023*. **24**, 16203 (2023).
4. Heydari, F. I. et al. Solvothermal synthesis of Polyvinyl pyrrolidone encapsulated, amine-functionalized copper ferrite and its use as a magnetic resonance imaging contrast agent. *PLoS One*. **20**, e0316221 (2025).
5. Gerzsenyi, T. B. et al. A simplified and efficient method for production of manganese ferrite magnetic nanoparticles and their application in DNA isolation. *Int. J. Mol. Sci.* **24**, 2156 (2023).
6. Maniotis, N., Gitsou, M. & Maragakis, M. Conjugating magnetic nanoparticles anisotropy to their dipolar interactions: effect on the hyperthermic losses index via micromagnetic simulations. *J. Magn. Magn. Mater.* **617**, 172843 (2025).
7. Nori, Z. Z. et al. Synthesis and characterization of a new gold-coated magnetic nanoparticle decorated with a thiol-containing dendrimer for targeted drug delivery, hyperthermia treatment and enhancement of MRI contrast agent. *J. Drug Deliv Sci. Technol.* **81**, 104216 (2023).
8. Karakatsanis, A. et al. Superparamagnetic iron oxide nanoparticles as the sole method for Sentinel node biopsy detection in patients with breast cancer. *Br. J. Surg.* **104**, 1675–1685 (2017).

9. Gupta, N., Jain, P., Rana, R. & Shrivastava, S. Current development in synthesis and characterization of nickel ferrite nanoparticle. *Mater. Today Proc.* **4**, 342–349 (2017).
10. Poon, K., Gupta, A., Hawkins, P. M. E. & Singh, G. Core-shell magnetic nanoparticles: Harnessing synergistic effects for MRI and magnetic hyperthermia. *Mater. Today Chem.* **44**, 102533 (2025).
11. Sreelekshmi, D., Adarsh, V. S. & Kumar, R. V. Anticancerous activity of Annona muricata-mediated cerium doped nickel ferrite spinel nanoparticles. *Mater. Chem. Phys.* **332**, 130138 (2025).
12. Zemlianskii, P. V., Kustov, A. L., Timofeeva, M. N. & Kustov, L. M. Microwave irradiation as an instrument for tuning of physicochemical and catalytic properties of MFe2O4 spinels. *Chem. Eng. Process. - Process. Intensif.* **208**, 110138 (2025).
13. Bayrakdar, H., Yalçın, O., Özüm, S. & Cengiz, U. Synthesis and investigation of small g-values for smart spinel ferrite nanoparticles. *J. Alloys Compd.* **869**, 159334 (2021).
14. Reddy, M. P. & Mohamed, A. M. A. One-pot solvothermal synthesis and performance of mesoporous magnetic ferrite MFe2O4 nanospheres. *Microporous Mesoporous Mater.* **215**, 37–45 (2015).
15. Azam, A. Microwave assisted synthesis and characterization of Co doped Cu ferrite nanoparticles. *J. Alloys Compd.* **540**, 145–153 (2012).
16. Ramesh, T. et al. Impact of ultrasonic-assisted co-precipitation synthesis and ultrasonication duration on Cobalt ferrite nanostructures: A comparative study of structural, morphological, optical and magnetic properties. *Inorg. Chem. Commun.* **174**, 114035 (2025).
17. Aoopngan, C. et al. Amine-Functionalized and Hydroxyl-Functionalized magnesium ferrite nanoparticles for congo red adsorption. *ACS Appl. Nano Mater.* **2**, 5329–5341 (2019).
18. Zhu, Y. & Wu, Q. Synthesis of magnetite nanoparticles by precipitation with forced mixing. *J. Nanoparticle Res.* **1**, 393–396 (1999).
19. Zain, U. et al. A comprehensive review on the synthesis of ferrite nanomaterials via bottom-up and top-down approaches advantages, disadvantages, characterizations and computational insights. *Coord. Chem. Rev.* **520**, 216158 (2024).
20. Rane, A. V., Kanny, K., Abitha, V. K. & Thomas, S. Methods for synthesis of nanoparticles and fabrication of nanocomposites. *Synthesis Inorg. Nanomaterials: Adv. Key Technol.* (Elsevier), 121–139. https://doi.org/10.1016/B978-0-08-101975-7.00005-1 (2018).
21. Gan, Y. X., Jayatissa, A. H., Yu, Z., Chen, X. & Li, M. Hydrothermal Synthesis of Nanomaterials. *J. Nanomater.* 8917013 (2020). (2020).
22. Torres-Gómez, N. et al. Shape tuning of magnetite nanoparticles obtained by hydrothermal synthesis: effect of temperature. *J. Nanomater.* **7921273** 2019 (2019).
23. Mizutani, N., Iwasaki, T., Watano, S., Yanagida, T. & Kawai, T. Size control of magnetite nanoparticles in hydrothermal synthesis by coexistence of lactate and sulfate ions. *Curr. Appl. Phys.* **10**, 801–806 (2010).
24. Ghosh Chaudhuri, R. & Paria, S. Core/shell nanoparticles: Classes, properties, synthesis mechanisms, characterization, and applications. *Chem. Rev.* **112**, 2373–2433 (2012).
25. Mahdavi, Z. & Rezvani, H. Keshavarz Moraveji, M. Core–shell nanoparticles used in drug delivery-microfluidics: a review. *RSC Adv.* **10**, 18280–18295 (2020).
26. Kargar, S., Elhamifar, D. & Zarnegaryan, A. Core–shell structured Fe_3O_4@SiO_2-supported IL/[Mo_6O_{19}]: A novel and magnetically recoverable nanocatalyst for the Preparation of biologically active dihydropyrimidinones. *J. Phys. Chem. Solids.* **146**, 109601 (2020).
27. Tahir, W. et al. Impact of silver substitution on the structural, magnetic, optical, and antibacterial properties of Cobalt ferrite. *Sci. Rep. 2023.* **131 13**, 1–23 (2023).
28. León Félix, L. et al. Structural and magnetic properties of core-shell Au/Fe_3O_4 nanoparticles. *Sci. Rep.* **2017 71 7**, 1–8 (2017).
29. Sharaf, E. M. et al. Synergistic antibacterial activity of compact silver/magnetite core-shell nanoparticles core shell against Gram-negative foodborne pathogens. *Front Microbiol* **13**, (2022).
30. Najafpoor, A. et al. Effect of magnetic nanoparticles and silver-loaded magnetic nanoparticles on advanced wastewater treatment and disinfection. (2020). https://doi.org/10.1016/j.molliq.2020.112640
31. Surendhiran, D., Sirajunnisa, A. & Tamilselvam, K. Silver–magnetic nanocomposites for water purification. *Environ. Chem. Lett.* **15**, 367–386 (2017).
32. Yu, Y. et al. Purifying water with silver nanoparticles (AgNPs)-incorporated membranes: recent advancements and critical challenges. *Water Res.* **222**, 118901 (2022).
33. Siddiqi, K. S., Husen, A. & Rao, R. A. K. A review on biosynthesis of silver nanoparticles and their biocidal properties. *J. Nanobiotechnology* 16, 1–28 (2018). (2018).
34. Marambio-Jones, C. & Hoek, E. M. V. A review of the antibacterial effects of silver nanomaterials and potential implications for human health and the environment. *J. Nanoparticle Res.* 12, 1531–1551 (2010). (2010).
35. Bruna, T., Maldonado-Bravo, F., Jara, P. & Caro, N. Silver nanoparticles and their antibacterial applications. *Int. J. Mol. Sci. 2021.* **22**, 7202 (2021).
36. Kumar, S. et al. Silver Micro-Nanoparticles - Properties, Synthesis, Characterization, and applications. *Silver Micro-Nanoparticles - Prop. Synth. Charact. Appl.* https://doi.org/10.5772/INTECHOPEN.92480 (2021).
37. Pinto, M. et al. Application of magnetic nanoparticles for water purification. *Environ. Adv.* **2**, 100010 (2020).
38. Hassan, A., Sorour, N. M., El-Baz, A. & Shetaia, Y. Simple synthesis of bacterial cellulose/magnetite nanoparticles composite for the removal of antimony from aqueous solution. *Int. J. Environ. Sci. Technol.* 16, 1433–1448 (2018). (2018).
39. Kunduru, K. R. et al. Nanotechnology for water purification: applications of nanotechnology methods in wastewater treatment. *Water Purif.* 33–74. https://doi.org/10.1016/B978-0-12-804300-4.00002-2 (2017).
40. Grün, A. L. et al. Impact of silver nanoparticles (AgNP) on soil microbial community depending on functionalization, concentration, exposure time, and soil texture. *Environ. Sci. Eur.* **31**, 1–22 (2019).
41. Xiu, Z. M., Zhang, Q. B., Puppala, H. L., Colvin, V. L. & Alvarez, P. J. J. Negligible particle-specific antibacterial activity of silver nanoparticles. *Nano Lett.* **12**, 4271–4275 (2012).
42. Shi, Y. et al. Magnetic properties of Cobalt ferrite nanoparticles synthesized by sol-gel method. *IOP Conf. Ser. Mater. Sci. Eng.* **73**, 012050 (2015).
43. Sivakumar, P., Ramesh, R., Ramanand, A., Ponnusamy, S. & Muthamizhchelvan, C. Synthesis and characterization of nickel ferrite magnetic nanoparticles. *Mater. Res. Bull.* **46**, 2208–2211 (2011).
44. Batlle, X. & Labarta, A. Finite-size effects in fine particles: magnetic and transport properties. *J. Phys. D Appl. Phys.* **35**, 201 (2002).
45. Ma, J. et al. Preparation of Cobalt ferrite nanoparticles via a novel solvothermal approach using divalent iron salt as precursors. *Mater. Res. Bull.* **48**, 214–217 (2013).
46. Aslibeiki, B. et al. Magnetic hyperthermia properties of CoFe2O4 nanoparticles: effect of polymer coating and interparticle interactions. *Ceram. Int.* **48**, 27995–28005 (2022).
47. Li, X. et al. Size-effect induced cation redistribution on the magnetic properties of well-dispersed $CoFe_2O_4$ nanocrystals. *J. Alloys Compd.* **841**, 155710 (2020).
48. Wang, J., Ren, F., Jia, B. & Liu, X. Solvothermal synthesis and characterization of $NiFe_2O_4$ nanospheres with adjustable sizes. *Solid State Commun.* **150**, 1141–1144 (2010).
49. Bernaoui, C. R. et al. Synthesis and characterization of $NiFe_2O_4$ nanoparticles as reusable magnetic nanocatalyst for organic dyes catalytic reduction: study of the counter anion effect. *Mater. Chem. Phys.* **292**, 126793 (2022).

50. Prieto, P. et al. XPS study of silver, nickel and bimetallic silver–nickel nanoparticles prepared by seed-mediated growth. *Appl. Surf. Sci.* **258**, 8807–8813 (2012).
51. Waldron, R. D. Infrared spectra of ferrites. *Phys. Rev.* **99**, 1727 (1955).
52. Zhou, B. et al. Rare-earth-mediated magnetism and magneto-optical Kerr effects in nanocrystalline $CoFeMn_{0.9}RE_{0.1}O_4$ thin films. *J. Magn. Magn. Mater.* **280**, 327–333 (2004).
53. Bruce, I. J. et al. Synthesis, characterisation and application of silica-magnetite nanocomposites. *J. Magn. Magn. Mater.* **284**, 145–160 (2004).
54. Kłodzińska, E. et al. Effect of zeta potential value on bacterial behavior during electrophoretic separation. *Electrophoresis* **31**, 1590–1596 (2010).
55. Pal, S., Tak, Y. K. & Song, J. M. Does the antibacterial activity of silver nanoparticles depend on the shape of the nanoparticle? A study of the gram-negative bacterium Escherichia coli. *Appl. Environ. Microbiol.* **73**, 1712–1720 (2007).
56. Fu, G., Vary, P. S. & Lin, C. T. Anatase TiO_2 nanocomposites for antimicrobial coatings. *J. Phys. Chem. B.* **109**, 8889–8898 (2005).
57. Mikhailova, E. O. Silver Nanoparticles: Mechanism of Action and Probable Bio-Application. *J. Funct. Biomater.* Vol. 11, Page 84 11, 84 (2020). (2020).
58. Neal, A. L. What can be inferred from bacterium-nanoparticle interactions about the potential consequences of environmental exposure to nanoparticles? *Ecotoxicology* **17**, 362–371 (2008).
59. Wu, G. et al. Evaluation of agar dilution and broth microdilution methods to determine the disinfectant susceptibility. *J. Antibiot.* 68, 661–665 (2015). (2015).
60. Abbaszadegan, A. et al. The effect of charge at the surface of silver nanoparticles on antimicrobial activity against Gram-Positive and Gram-Negative bacteria: A preliminary study. *J. Nanomater.* **2015**, 8. https://doi.org/10.1155/2015/720654 (2015).
61. Tippayawat, P., Phromviyo, N., Boueroy, P. & Chompoosor, A. Green synthesis of silver nanoparticles in aloe vera plant extract prepared by a hydrothermal method and their synergistic antibacterial activity. *PeerJ* (2016). (2016).
62. Wang, L., Hu, C. & Shao, L. The antimicrobial activity of nanoparticles: present situation and prospects for the future. *Int. J. Nanomed.* **12**, 1227–1249 (2017).
63. Jo, D. H., Kim, J. H., Lee, T. G. & Kim, J. H. Size, surface charge, and shape determine therapeutic effects of nanoparticles on brain and retinal diseases. *Nanomed. Nanatechnol. Biol. Med.* **11**, 1603–1611 (2015).
64. Cheon, J. Y., Kim, S. J., Rhee, Y. H., Kwon, O. H. & Park, W. H. Shape-dependent antimicrobial activities of silver nanoparticles. *Int. J. Nanomed.* **14**, 2773–2780 (2019).
65. Sharma, V. K. & Zboril, R. Silver nanoparticles in natural environment: Formation, Fate, and toxicity. 239–258 (2017). https://doi.org/10.1007/978-981-10-5864-6_10
66. Wei, M., Huang, A. C., Shu, C. M. & Zhang, L. Thermal decomposition and nonisothermal kinetics of monoethanolamine mixed with various metal ions. *Sci. Rep. 2019.* **91 9**, 1–9 (2019).
67. Chi, S. & Rochelle, G. T. Oxidative degradation of monoethanolamine. *Ind. Eng. Chem. Res.* **41**, 4178–4186 (2002).
68. Rijo, P. et al. Glycyrrhizic acid nanoparticles subside the activity of Methicillin-Resistant Staphylococcus aureus by suppressing PBP2a. *Pharmaceuticals* **17**, 589 (2024).
69. Hassan, A. et al. Inhibition mechanism of Methicillin-Resistant Staphylococcus aureus by zinc oxide nanorods via suppresses Penicillin-Binding protein 2a. *ACS Omega*. **8**, 9969–9977 (2023).

Author contributions

Conceptualization, L.V., E.Sz-D. and A.M.I.; methodology, L. D., A.M.I., O.A., K.K., E.Sz-D. and F. K; software, M.N. and B.V.; formal analysis, F.K., M.N., O.A. and L.D.; resources, M.N. and B.V.; data curation, L.V., E.Sz-D. and A.M.I.; writing—original draft preparation L.V., E.Sz-D. and A.M.I.; writing—review and editing, M.N., B.V. and E.Sz-D.; visualization, L.V. and E.Sz-D.; supervision, L. V. and E.Sz-D. All authors have read and agreed to the published version of the manuscript.

Funding

This paper was supported by the János Bolyai Research Scholarship of the Hungarian Academy of Sciences. Supported by the University Research Scholarship Program of the Ministry for Culture and Innovation from the source of the National Research, Development and Innovation Fund.

Declarations

Competing interests

The authors declare no competing interests.

Additional information

Supplementary Information The online version contains supplementary material available at https://doi.org/10.1038/s41598-025-33520-7.

Correspondence and requests for materials should be addressed to E.S.-D. or L.V.